

4. A.C. Ulusoy, P. Song, W.T. Khan, M. Kaynak, N. Tillack, and J.D. Cressler, A SiGe D-band low-noise amplifier utilizing gain-boosting technique, *IEEE Microw Wirel Compon Lett* 25 (2015), 61–63.
5. H. Hsieh, P. Wu, C. Jou, F. Hsueh, and G. Huang, 60 GHz high-gain low-noise amplifiers with a common-gate inductive feedback in 65nm CMOS, *Proc IEEE Radio Freq Integr Circuit Symp* (2011), 1–4.
6. B. Razavi, *Design of analog CMOS integrated circuit*, McGraw-Hill, New York, NY, 2001, 232–235.
7. D.H. Seo, J.Y. Lee, and T.Y. Yun, Active and passive combined mixer for low flicker noise and low dc offset, *IEEE Microw Wirel Compon Lett* 25 (2015), 463–465.
8. B. Guo, H. Wang, and G. Yang, A wideband merged CMOS active mixer exploiting noise cancellation and linearity enhancement, *IEEE Trans Microw Theory Tech* 62 (2014), 2084–2091.
9. W.J. Jung, S.M. Lim, J.H. Lee, K.H. Nam, J.E. Jang, and J.S. Park, A 5 dB NF 100 kHz 1/f corner and 35 dBm OIP3 down conversion mixer using dynamic current injection and derivative superposition method, *Microw Opt Tech Lett* 58 (2016), 1720–1723.
10. H.K. Chiou, K.C. Lin, W.H. Chen, and Y.Z. Juang, A 1-V 5-GHz self-bias folded-switch mixer in 90-nm CMOS for WLAN receiver, *IEEE Trans Circuit Syst I* 59 (2012), 1215–1227.
11. J. Xu, C.E. Saavedra, and G. Chen, A 12 GHz-bandwidth CMOS mixer with variable conversion gain capability, *IEEE Microw Wirel Compon Lett* 21 (2011), 565–567.
12. S.K. Hampel, O. Schmitz, M. Tiebout, and I. Rolfes, Inductorless low-voltage and low-power wideband mixer for multistandard receivers, *IEEE Trans Microw Theory Tech* 58 (2010), 1384–1390.
13. S.S.K. Ho, and C.E. Saavedra, A CMOS broadband low-noise mixer with noise cancellation, *IEEE Trans Microw Theory Tech* 58 (2010), 1126–1132.

© 2016 Wiley Periodicals, Inc.

## EVALUATION OF A TUMOR DETECTION MICROWAVE SYSTEM WITH A REALISTIC BREAST PHANTOM

Maria Koutsoupidou,<sup>1</sup> Irene S. Karanasiou,<sup>1,5</sup>  
Constantine G. Kakoyiannis,<sup>2</sup> Evangelos Groumpas,<sup>1</sup>  
Christophe Conessa,<sup>3</sup> Nadine Joachimowicz,<sup>3</sup> and  
Bernard Duchêne<sup>4</sup>

<sup>1</sup>Institute of Communication and Computer Systems, National Technical University of Athens, Greece; Corresponding author: mkouts@esd.ece.ntua.gr

<sup>2</sup>Institute of Communication and Computer Systems, National Technical University of Athens, Greece

<sup>3</sup>Laboratoire Génie Electrique et Electronique de Paris (GeePs): CNRS - CentraleSupélec - UPMC - Univ Paris-Sud), Université Paris-Saclay, 91190 Gif-sur-Yvette, France

<sup>4</sup>Laboratoire des Signaux et Systèmes (L2S: CNRS - CentraleSupélec - Univ Paris-Sud), Université Paris-Saclay, 91190 Gif-sur-Yvette, France

<sup>5</sup>Hellenic Military University, Greece

Received 25 May 2016

**ABSTRACT:** In this article, we describe recent advances regarding a novel microwave imaging system intended to be used for in-depth inspection of breast tissues. The system is made of a circular five-element antenna array surrounding the breast that can be moved axially to perform a scan of the entire breast. The performance of the system is studied, both numerically and experimentally with a realistic anthropomorphic breast phantom, as a proof of concept of its fast and accurate screening ability to detect tumor-like inclusions. © 2016 Wiley Periodicals, Inc. *Microw Opt Technol Lett* 59:6–10, 2017; View this article online at [wileyonlinelibrary.com](http://wileyonlinelibrary.com). DOI 10.1002/mop.30212

**Key words:** microwave imaging; breast cancer detection; planar antenna array; breast phantoms

## 1. INTRODUCTION

Microwave imaging (MWI) has attracted significant research interest as a novel modality for breast cancer detection that presents important advantages over other techniques currently applied in clinical practice. Indeed, mammography is the subject of a controversy regarding its safety, due to the ionizing nature of X-rays, and it also suffers from a high missed detection and false alarm rate [1,2] and of a procedure that can be uncomfortable, even painful, for the patient. Among other clinical tools for breast cancer diagnosis, the most prevalent are ultrasound imaging and MRI. However, ultrasounds offer only supplementary information with a low sensitivity for young patients [2], whereas MRI is an expensive option for annual screening.

Microwave technology, on the other hand, offers an alternative modality for a low-cost and non-ionizing diagnostic tool able to detect malignancies surrounded by healthy breast tissues and benign tumors [3]. Usually a MWI system is made of an array of antennas that illuminate the breast and collect the energy scattered by the latter. Then, a measurement chain converts this energy into data that are fed to an inverse scattering or a radar-based algorithm in charge of building up a map of the dielectric permittivity within the breast [4–6].

During the last two decades, various MWI systems have been developed [3,7–9] and have attempted to address the issues that must be solved before a clinical application, i.e., a fast scanning and a sub-centimeter image resolution [10]. They differ from the hardware (antennas, operating bandwidth and array setup) as well as the software (the inversion algorithm used to build up the image) point of view.

In this article, recent advances in the development of a prototype imaging system are presented. The present study focuses on the design of an appropriate antenna configuration able to efficiently and quickly detect tumor-mimicking structures in a realistic phantom. The ability of the system to detect small tumors is investigated, both at numerical and experimental levels, by comparing its response in the presence and in the absence of tumor-like inclusions in a numerical model and in a realistic anthropomorphic breast phantom. The scope of this article does not include the description of the performance of the entire system and, particularly, that of the measurement chain and of the image reconstruction algorithm.

## 2. SYSTEM ANALYSIS AND EVALUATION

The MWI system is based upon a 5-element array of uniplanar elliptical antennas [11] arranged around the breast on a circular substrate that moves vertically along the axis perpendicular to the plane of the setup. The antennas are equally spaced and placed as displayed in Figure 1(a). Such antennas have been chosen as they behave as small dipoles. Their radiation pattern has a toroidal shape around the elliptical patch, which reduces significantly the mutual coupling between the array elements. Moreover, despite their dipole-like radiation characteristics and their small size (4 cm × 5 cm), these antennas exhibit an ultra-wideband behavior and a low cut-off frequency: their operating bandwidth extents from 1.53 GHz to 3.33 GHz, which represents a fractional bandwidth of 74%. This frequency range yields a good trade-off between the penetration depth in the breast and the image resolution that can be expected. Furthermore, the small number of array elements yields a fast scanning of the region of interest and the system is designed to operate in the air so that there is no need of a matching medium.

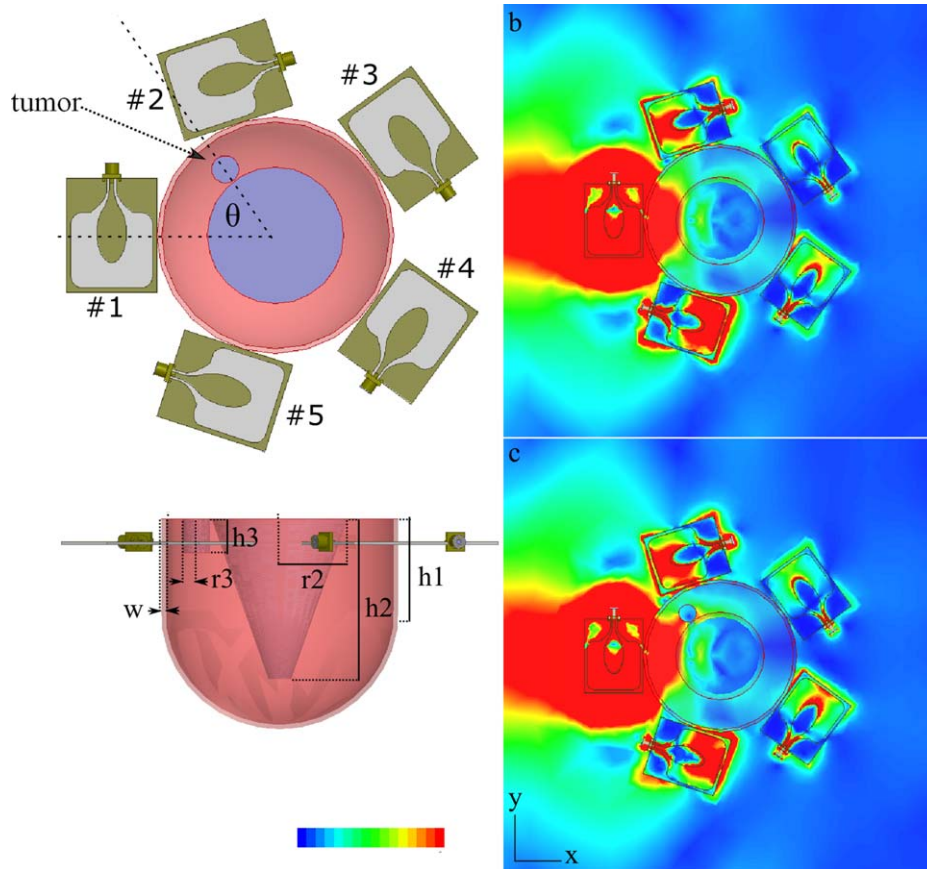


**Figure 1** (a) Top and side views of the simulated setup with the antenna array surrounding the breast model and electric field distribution when antenna #1 operates at 1.5 GHz (b) without and (c) with the tumor. [Color figure can be viewed at [wileyonlinelibrary.com](https://onlinelibrary.wiley.com)]

### 2.1. Numerical Model

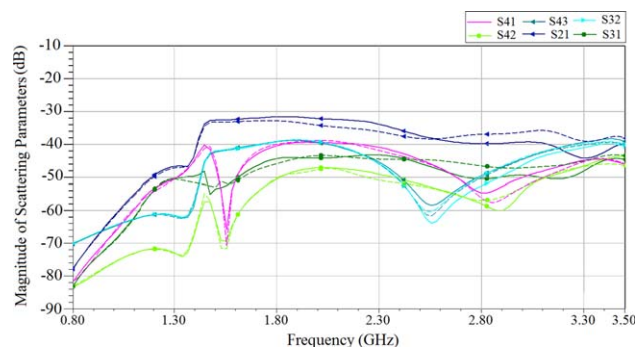
As a first step, the array setup described above was modeled by means of ANSYS HFSS in the 0.8–3.5 GHz frequency range and tested on a numerical breast phantom. The breast phantom [see Fig. 1(a)] is made of a cylinder, whose height and radius are respectively 4 cm and 5.2 cm, followed by a hemispherical part. It comprises several layers whose dielectric properties mimic that of various breast tissue types at a frequency of 1.5 GHz [12–14], i.e., a skin layer (thickness  $w = 2$  mm, relative permittivity  $\epsilon_r = 39.4$ , conductivity  $\sigma = 1.07$  S/m) surrounding a fat layer (radius  $r_1 = 5$  cm,  $\epsilon_r = 5.32$ ,  $\sigma = 0.07$  S/m) that includes a glandular-type part of conical shape (base radius  $r_2 = 3$  cm, height  $h_2 = 7$  cm,  $\epsilon_r = 58.6$ ,  $\sigma = 1.32$  S/m). A small optional cylindrical part (radius  $r_3 = 5$  mm, height  $h_3 = 15$  mm), that mimics a tumor, can also be included in the fat layer; it is then located in contact with the glandular inclusion at an angle  $\theta = 52^\circ$  from the horizontal axis [see Fig. 1(a)] and its dielectric properties are chosen to be 8% higher than those of the glandular tissue, which lies within the margins reported in the literature [15,16].

Figure 1 displays the electric field radiated by antenna #1 in the  $xy$ -plane at a frequency of 1.5 GHz, in the presence [Fig. 1(b)] and in the absence [Fig. 1(c)] of tumor. It can be observed that, at this frequency, despite the high loss level of the glandular part, the field penetrates through the latter to the center of the phantom and that the five antennas provide irradiation of the whole cross-section. It can be also observed in Figure 1(c) that the tumor distorts the electric field and scatters energy towards antenna #2. Figure 2 displays some of the scattering parameters of the antenna array as functions of the frequency. It can be

seen that from 1.5 GHz to 2.5 GHz, the tumor attenuates the energy received by antennas #2 and #3 by a value in between 1 and 5 dB and, above 2.5 GHz, the signal is scattered towards these antennas, which enhances the values of  $S_{21}$  and  $S_{31}$ .

### 2.2. Experimental Setup

In a second step, the array setup has been realized on a substrate made of a Styrofoam ring and tested on a realistic anthropomorphic breast phantom. For that purpose, four of the antennas have been connected to a four-port vector network analyzer, while the fifth one (antenna #5) was terminated by a  $50\ \Omega$  coaxial load.



**Figure 2** Scattering parameters  $S_{mn}$  of the antenna array in the presence of the breast phantom with (dashed lines) and without (solid lines) tumor. [Color figure can be viewed at [wileyonlinelibrary.com](https://onlinelibrary.wiley.com)]

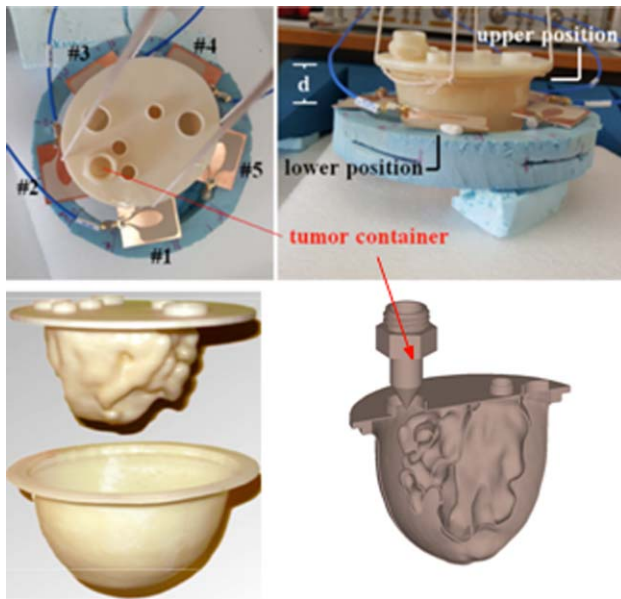


**Figure 3** The experimental setup with (top) the antenna array arranged on a Styrofoam hoop around the breast phantom and (bottom) photograph and cross-sectional view of the latter. [Color figure can be viewed at [wileyonlinelibrary.com](http://wileyonlinelibrary.com)]

As for the phantom, it is made of a 3D structure realized by 3D printing, as it has been done in Ref. [17]. In this reference appears a link to a numerical phantom repository where a STL file corresponding to an anatomically realistic MRI-derived breast phantom can be found. However, the latter has dielectric properties very far from those of a real breast, since it consists of a single cavity with thick walls made of printable material. This is the reason why we have modified the file in order to create two separate cavities whose shapes are very similar to realistic distributions of fibro-glandular and adipose tissues [18]. Figure 3(bottom) displays cross-sectional views and photographs of this structure that show its modularity. There are three parts: two shells fixed to an elliptical plate that form two cavities intended to be filled up with tissue mimicking mixtures and a removable tumor mimicking part that can be placed at different

locations within the phantom. The structure is made of 1.5-mm-thick ABS coated with epoxy resin in order to avoid leakage problems. Its dielectric properties, measured at 2.5 GHz, are  $\epsilon_r = 3.06$  and  $\sigma = 0.08$  S/m. The

As for the phantom, it is made of a 3D structure realized by 3D printing, as it has been done in Ref. 17. In this reference appears a link to a numerical phantom repository where a STL file corresponding to an anatomically realistic MRI-derived breast phantom can be found. However, the latter has dielectric properties very far from those of a real breast, since it consists of a single cavity with thick walls made of printable material. This is the reason why we have modified he file in order to create two separate cavities whose shapes are very similar to realistic distributions of fibro-glandular and adipose tissues [18]. Figure 3 (bottom) displays cross-sectional views and photographs of this structure that show its modularity. There are three parts: two shells fixed to an elliptical plate that form two cavities intended to be filled up with tissue mimicking mixtures and a removable tumor mimicking part that can be placed at different locations within the phantom. The structure is made of 1.5-mm-thick ABS coated with epoxy resin in order to avoid leakage problems. Its dielectric properties, measured at 2.5 GHz, are  $\epsilon_r = 3.06$  and  $\sigma = 0.08$  S/m. The outer shell is 10 cm high with elliptical base axes = 9 cm  $\times$  11 cm, whereas the tumor mimicking inclusion is made of a cylindrical part (radius = 7 mm, height = 1.4 cm) followed by a conical cap (height = 1.6 cm). It can be noted that this phantom is intended to become a reference breast phantom dedicated to the test of MWI systems in the framework of the COST Action 1301 MiMed [18].

Although other recipes can be found [19,20], the mixtures mimicking the tumor (*T*), the breast fat (*F*) and the glandular tissue (*G*), intended to fill up the removable inclusion and the outer and inner cavities, respectively, are made of distilled water (*w*), sugar (*sr*), agar (*a*) and salt (*st*) in various proportions [21], i.e.,  $F = 47\% w + 47\% sr + 6\% a$ ,  $G = 71\% w + 14.5\% sr + 14.5\% a$  and  $T = 71\% w + 14.5\% sr + 14.5\% a + 10 \text{ g/L } st$ . The mixtures are kept at room temperature in a liquid form and their properties, measured at 2 GHz, are *F*:  $\epsilon_r = 20$ ,  $\sigma = 1$  S/m, *G*:  $\epsilon_r = 55$ ,  $\sigma = 1.9$  S/m and *T*:  $\epsilon_r = 55$ ,  $\sigma = 2.1$  S/m. It can be noted that the permittivity of the fatty tissue is relatively high compared to standard values ( $\epsilon_r \approx 5$ ), but this compensates

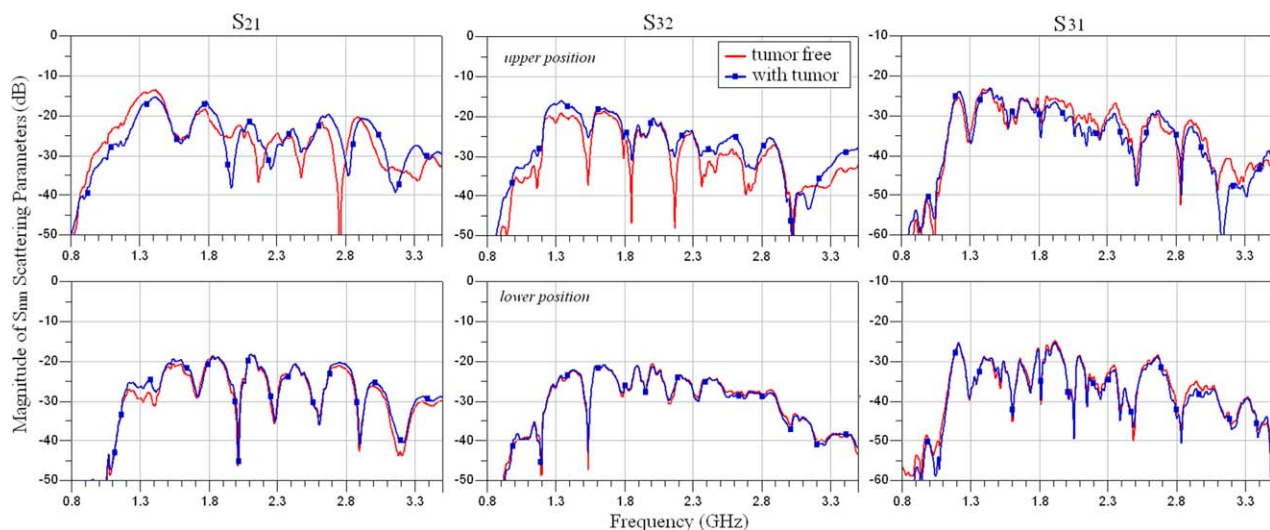


**Figure 4** Magnitudes of the  $S_{21}$ ,  $S_{32}$  and  $S_{31}$  scattering parameters when the antenna array is placed at the (top) upper and (bottom) lower positions with (blue line) and without (red line) tumor. [Color figure can be viewed at [wileyonlinelibrary.com](http://wileyonlinelibrary.com)]



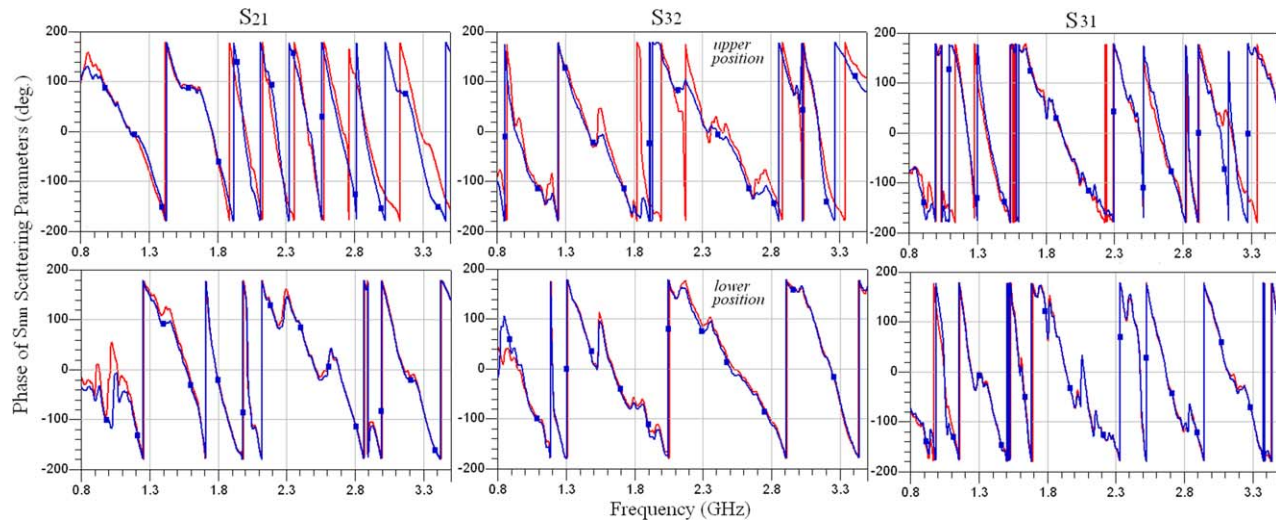


**Figure 5** Phases of the  $S_{21}$ ,  $S_{32}$  and  $S_{31}$  scattering parameters when the antenna array is placed at the (*top*) upper and (*bottom*) lower positions with (blue line) and without (red line) tumor. [Color figure can be viewed at [wileyonlinelibrary.com](http://wileyonlinelibrary.com)]

somewhere the low permittivity value of the ABS compared to that of the skin.

### 3. MEASUREMENTS

The measurements are performed with the antenna array at two different heights, at a distance  $d = 2$  cm apart from each other [Fig. 3(*top-right*)]. At the upper position the array plane intersects the tumor-like inclusion, while at the lower one it lays beneath the latter. At both positions, the antenna array scattering parameters are measured with and without the removable tumor-like inclusion.

Figures 4 and 5 display respectively the magnitude and phase of some of the scattering parameters as functions of the frequency in the 0.8–3.5 GHz range. All the parameters follow the same scheme: at the lower position the magnitude and phase of  $S_{mn}$  are the same in the presence and in the absence of the tumor-like inclusion, while at the upper position there is a clear difference of 1 to 5 dB in magnitude and  $10^\circ$  to  $90^\circ$  in phase within selected bands. In the latter case, the presence of the tumor significantly alters the magnitude of  $S_{21}$  within the whole bandwidth and shifts its phase up to  $20^\circ$  and  $90^\circ$  in the 1.9–2.4 GHz band and above 2.7 GHz, respectively. As antenna #3 receives also the energy scattered by the tumor, the presence of the latter increases by 3 to 5 dB the magnitude of  $S_{32}$  and significantly alters its phase within the whole bandwidth, while the magnitude of  $S_{31}$  decreases by 1 to 3 dB in the 1.8–2.8 GHz band and its phase is shifted by  $10^\circ$  to  $90^\circ$  in the 3.0–3.4 GHz range. Finally, as the inclusion lies closer to antennas #1, #2 and #3 than to the other ones, the scattering parameters relative to the former are more affected than those relative to the latter that are little disturbed.

### 4. CONCLUSION

In this article, we propose a 5-element circular antenna array surrounding the breast that can move vertically along its axis to be used as part of a microwave breast imaging system. The configuration in question combines three important features required for clinical use: (i) an ultra-wideband behavior of the antennas with a low cut-off frequency, (ii) no need for a matching medium and (iii) a small number of antennas that allows fast horizontal scanning.

The study presented herein is a proof of concept: when tested on a realistic anthropomorphic breast phantom, the system has been proven to detect the presence of a tumor-like inclusion when the latter intersects the antenna array plane, but, as expected, it does not sense it otherwise. Further studies are required, particularly on the ability of the system to detect inclusions deeply embedded in the glandular part of the breast and on the image resolution that can finally be expected after data processing with an inverse scattering or a radar-based algorithm. This resolution will depend upon the inversion algorithm, upon the operating frequency range and upon the vertical scanning step used to build up a tomographic image of the whole breast. As it defines the total volume of data, this step should result from a tradeoff between the expected resolution and the data collection and processing speed.

### ACKNOWLEDGEMENT

The authors acknowledge the University of Wisconsin-Madison for the provision of the original STL file. This work has been supported by COST Action TD1301, MiMed.

### REFERENCES

1. A. Bleyer, and H.G. Welch, Effect of three decades of screening mammography on breast-cancer incidence, *N Engl J Med* 376 (2012), 1998–2005.
2. E. Fallenberg, C. Dromain, F. Diekmann, F. Engelken, M. Krohn, J.M. Singh, B. Ingold-Heppner, KJ Winzer, U Bick, and D.M. Renz, Contrast-enhanced spectral mammography versus MRI: Initial results in the detection of breast cancer and assessment of tumour size, *Eur Radiol* 24 (2014), 256–264.
3. G.A. Ybarra, Q.H. Liu, J.P. Stang, and W.T. Joines, Microwave breast imaging, in *Emerging Technology in Breast Imaging and Mammography*, In: J. Suri et al. (Eds.), American Scientific Publishers, Valencia, CA, USA, 2007.
4. S. Raghavan and M. Ramaraj, An overview of microwave imaging towards for breast cancer diagnosis, *Proc PIERS Moscow* (2012), 627–630.
5. X. Li, S.K. Davis, S.C. Hagness, D.W. van der Weide, and B.D. Van Veen, Microwave imaging via space-time beamforming: Experimental investigation of tumor detection in multilayer breast phantoms, *IEEE Trans Microw Theory Tech* 52 (2004), 1856–1865.
6. M. Azghani, P. Kosmas, and F. Marvasti, Microwave imaging based on compressed sensing using adaptive thresholding, *Proc 8th EuCAP, The Hague* (2014), 699–701.

7. S. M. Aguilar, et al. Multiband miniaturized patch antennas for a compact, shielded microwave breast imaging array, *IEEE Trans Antenna Propag* 62 (2014), 1221–1231.
8. L. Lizzi et al. Synthesis of a wideband antenna array for microwave imaging applications, in *Proc. 5th EuCAP, Rome* (2011), 1938–1941.
9. S. Tiang et al. Wide-slot antenna for breast imaging applications, in *Proc. IEEE SAS, Queenstown* (2014), 1–5.
10. T.M. Grzegorzczak, P.M. Meaney, P.A. Kaufman, R.M. di Florio-Alexander, and K.D. Paulsen, Fast 3-D tomographic microwave imaging for breast cancer detection, *IEEE Trans Med Imaging* 31 (2012), 1584–1592.
11. M. Koutsoupidou, E. Groumpas, C.G. Kakoyiannis, I.S. Karanasiou, M. Gargalakos, and N. Uzunoglu, A microwave breast imaging system using elliptical uniplanar antennas in a circular-array setup, in *Proc. IEEE IST, Macau* (2015), 1–4.
12. C. Gabriel, S. Gabriel, and E. Corthout, The dielectric properties of biological tissues: I. Literature survey, *Phys Med Biol* 41 (1996), 2231–2249.
13. S. Gabriel, R. Lau, and C. Gabriel, The dielectric properties of biological tissues: II. Measurements in the frequency range 10 Hz to 20 GHz & III. Parametric models for the dielectric spectrum of tissues, *Phys Med Biol* 41 (1996), 2251–2293.
14. D. Andreuccetti, R. Fossi, and C. Petrucci, Calculation of the dielectric properties of body tissues in the 10 Hz–100 GHz range. Available at: <http://niremf.ifac.cnr.it/tissprop/htmlclie/htmlclie.php>.
15. M. Lazebnik, et al. A large-scale study of the ultrawideband microwave dielectric properties of normal, benign and malignant breast tissues obtained from cancer surgeries, *Phys Med Biol* 52 (2007), 6093–6115.
16. M. Lazebnik, et al. A large-scale study of the ultrawideband microwave dielectric properties of normal breast tissue obtained from reduction surgeries, *Phys Med Biol* 52 (2007), 2637–2656.
17. M. Burfeindt, et al. MRI-derived 3-D-printed breast phantom for microwave breast imaging validation, *IEEE Antenna Wirel Propag Lett* 11 (2012), 1610–1613.
18. N. Joachimowicz, B. Duchêne, C. Conessa, and O. Meyer, Easy-to-produce adjustable realistic breast phantoms for microwave imaging, in *Proc. 10th EuCAP, Davos* (2016), 2892–2895.
19. M. O'Halloran et al. Development of anatomically and dielectrically accurate breast phantoms for microwave imaging applications, in *Proc. SPIE 9077* (2014), 0Y1–0Y7.
20. N. Joachimowicz, C. Conessa, T. Henriksson, and B. Duchêne, Breast phantoms for microwave imaging, *IEEE Antenna Wirel Propag Lett* 13 (2014), 1333–1336.
21. M. Jalilvand, X. Li, L. Zwiello, and T. Zwick, Ultra wideband compact near-field imaging system for breast cancer detection, *IET Microw Antenna Propag* 9 (2015), 1009–1014.

© 2016 Wiley Periodicals, Inc.

## MILLIMETRE WAVE WIDEBAND LOW-LOSS WAVEGUIDE-TO-SUBSTRATE INTEGRATED WAVEGUIDE TRANSITION

J. Ross Aitken and Jiasheng Hong

Institute of Sensors, Signals and Systems, Heriot-Watt University, Edinburgh, United Kingdom; Corresponding author: ross.aitken@theiet.org

Received 1 June 2016

**ABSTRACT:** A wideband Ka-band waveguide-to-substrate integrated waveguide transition is presented based on a multi-section transformer approach. We designed our transition by successfully adapting multi-section inhomogeneous waveguide transformer theory to match a substrate integrated waveguide feedline to a standard waveguide flange, which offers more degrees of freedom than current design methods in

the state of the art. We subjected our transition to a simulated tolerance analysis and have found the transition to be robust when fabrication errors are considered. We validated these simulations by measuring a back-to-back waveguide-to-substrate integrated waveguide transition, where there is very good agreement between measured and simulated results. Moreover, an insertion loss of  $-0.48$  dB was measured at the center frequency of the required operating range. © 2016 Wiley Periodicals, Inc. *Microwave Opt Technol Lett* 59:10–12, 2017; View this article online at [wileyonlinelibrary.com](http://wileyonlinelibrary.com). DOI 10.1002/mop.30214

**Key words:** rectangular waveguide; substrate integrated waveguide; millimetre wave; tolerance study

### 1. INTRODUCTION

There is a growing interest and need to connect low-cost millimeter wave substrate integrated waveguide (SIW) components such as filters and diplexers to waveguide (WG) antenna systems. This requires a suitable low loss WG-to-SIW transition. At present, there are two main WG-to-SIW transitions discussed in the literature. The first is the aperture coupled type, which works by essentially radiating an SIW signal through coupling apertures or equivalent into a WG flange [1–4]. However transitions of this type exhibit high losses and are not ideal for use on millimeter wave systems as low insertion loss is a key requirement. For example, in Refs. 2,4 the measured insertion loss of aperture coupled transitions at Ka-band frequencies were found to be  $-1.5$  dB and  $-1.4$  dB, respectively, which is unsuitable. The second kind consists of designing a multi-section transformer to match the SIW circuit to a WG flange [5–7]. More promising insertion loss values have been reported in Ref. 5 using this type of transition, where an insertion loss of  $-0.68$  dB is quoted over the 30–50 GHz range. In this letter, we present a low-loss three section Ka-band WG-to-SIW transition based on the multi-section transformer approach. The transition is required to match a proof of concept SIW diplexer operating in the 31–37.5 GHz range to a standard WG 22 flange with a minimum passband return loss of  $-15$  dB.

### 2. TRANSITION DESIGN

Due to the equivalence between SIW and dielectric-filled WG, we can design the transition by considering it entirely as an inhomogeneous multi-section WG transformer problem. That is, our aim is to match a dielectric-filled WG to an arbitrary section of WG. In this way, we can successfully adapt inhomogeneous WG transformer theory such as that in Ref. 8 to design the transition using computer optimization techniques. The diplexer is constructed from Rogers RT 5880 which has a dielectric constant of 2.2 and a height of 1.574 mm. Moreover, the width of the input/output feedlines on the diplexer corresponds to a cut-off frequency of 24.4 GHz. In this case, to ensure a sufficient match was obtained over the operating range of the diplexer, a three section transformer structure was required. When compared to the four-section design in Ref. [5] where only two of the four sections of the transition are treated inhomogeneously, and the designs in Refs. [6,7] where all sections of the transition are treated homogeneously, this method offers more degrees of freedom for finding the optimum design.

### 3. RESULTS AND DISCUSSION

The simulated lossless frequency response of the transition can be seen in Figure 1 where a return loss of  $-23.8$  dB is obtained over the required 31–37.5 GHz operating range. One factor limiting the bandwidth of the transition is the cut-off frequency of the SIW feedline, as close to cut-off there is a large change of